Large-Angle-of-Attack Viscous Hypersonic Flows over Complex Lifting Configurations

Bilal A. Bhutta* and Clark H. Lewis†
VRA, Inc., Blacksburg, Virginia 24060

A new three-dimensional PNS scheme has been developed to study perfect-gas and equilibrium-air viscous hypersonic flows over complex three-dimensional configurations. This three-dimensional PNS scheme is unconditionally timelike in the subsonic as well as the supersonic flow regions and does not require any sublayer approximation. A predictor-corrector solution scheme and different grid-generation algorithms have been used along with an implicit shock-fitting scheme to predict the three-dimensional flowfields around some typical lifting configurations. A new fourth-order accurate smoothing approach has also been developed and used to enhance solution accuracy. The results show that substantial three-dimensional crossflow effects exist in the predicted flowfields, which need to be appropriately treated. Furthermore, the grid-generation result shows that for three-dimensional geometries with convex cross sections a slightly modified variation of a body-normal grid-generation scheme shows the best characterstics. The results also show that, for such complex configurations, the type of gas model used has a substantial effect on the predicted flowfield.

Nomenclature

M	= Mach number
n	= iteration number
P,p	= static pressure
Pr	= Prandtl number
PW	= wall pressure
$PINF$	= freestream static pressure, p_∞
QW	= total wall heat-transfer rate
Re	= Reynolds number, $(\rho VRn)/\mu$
RN,Rn	= nose radius
T	= static temperature
u	= x-component of velocity
v	= y-component of velocity
w	= z-component of velocity
X,x	= coordinate along body axis
α	= angle of attack
ϵ	= M_∞/Re_∞
ξ_1	= marching or streamwise coordinate
ξ_2	= coordinate measured from the body to the outer bow shock
ξ_3	= coordinate measured from the windward to the leeward side
ρ	= mixture density
ϕ	= circumferential angle measured from the windward side

Superscripts

n	= index for iteration
j	= index in ξ_1 direction

Subscripts

,	= represents partial derivative
∞	= freestream quantity
j,k,l	= indicial notation representing 1, 2, and 3

Presented as Paper 89-0269 at the AIAA 27th Aerospace Sciences Meeting, Reno, NV, Jan. 9-12, 1989; received Jan. 30, 1989, revision received July 18, 1989.

*Chief Scientist. Member AIAA.
†President. Associate Fellow AIAA.

Introduction

In the last few years, significant advances have been made in the field of computational fluid dynamics (CFD). The existing computational methodology for predicting hypersonic external flows over three-dimensional geometries consists of Navier-Stokes (NS), parabolized Navier-Stokes (PNS), and viscous shock-layer (VSL) schemes. The existing Navier-Stokes schemes[1-3] are typically very time consuming and not well suited for various parametric studies required for design and analysis purposes. On the other hand, the existing noniterative PNS schemes[4-9] suffer from instabilities and inaccuracies. Apart from being noniterative, such PNS schemes require a substantial approximation in the way the subsonic sublayer region is treated.[6,7] There are generally large global conservation-of-mass (as well as momentum and energy) errors associated with these methods, which originate from the basic noniterative nature of these PNS schemes. The existing three-dimensional VSL schemes[10-14] have a basic limitation of being parabolic in the crossflow direction and, consequently, cannot march through crossflow separated regions. This prevents the VSL schemes from accurately predicting the complete flowfield over complex lifting configurations, which may experience strong crossflow separation either due to a large-angle-of-attack condition or simply due to the three-dimensional nature of the geometry. However, even under these conditions the flowfield in the nose region is attached, and the VSL schemes represent an accurate and efficient way of generating the nose solutions for starting other (more accurate) afterbody methods that can treat crossflow separation (such as the PNS schemes).

Over the last several years we have been actively developing a new and powerful parabolized Navier-Stokes solution scheme[15-22] for three-dimensional hypersonic flows. This three-dimensional PNS scheme uses a general curvilinear coordinate system and is unconditionally timelike in the subsonic as well as the supersonic flow regions. Due to its unconditionally timelike character, this PNS scheme does not require any sublayer approximation.[17,18] The original axisymmetric formulation of this new PNS scheme was presented in 1985 by Bhutta and Lewis[15,16] for perfect-gas as well as nonequilibrium-air flows. The three-dimensional moderate-angle-of-attack (<5 deg) modifications of this scheme were done by Bhutta and Lewis[17] and Bhutta et al.[22] Recently, Bhutta and Lewis[20,21] presented their extensions of this three-dimensional scheme to large-angle-of-attack (≥ 20 deg) hypersonic flows.

Their work covered perfect-gas, equilibrium-air, and nonequilibrium-air gas models. However, these studies dealt with only simple multiconic configurations which were easily modeled using a cylindrical grid-generation algorithm.

In this paper we present our modifications of the three-dimensional PNS scheme of Bhutta and Lewis[15-21] and Bhutta et al.[22] to study perfect-gas and equilibrium-air hypersonic flows over three-dimensional lifting configurations. We have modified this PNS scheme to include different grid-generation schemes in order to better model the three-dimensional geometries. The vehicle geometries considered in this study have convex cross sections and are representative of a large class of hypersonic flight vehicles of current interest. In this study, we have implemented and used the new implicit shock-fitting scheme of Bhutta and Lewis.[20-21] In this fully implicit and crossflow-coupled shock-fitting scheme, the bow shock shape is accurately predicted as the solution marches down the body. Furthermore, we have also used the recently developed predictor-corrector solution scheme of Bhutta and Lewis.[20-21] This predictor-corrector scheme was originally developed to treat the strong crossflow coupling effects in and around the crossflow separated region. However, the present study shows that this predictor-corrector solution scheme is also very helpful and desirable for predicting the complex three-dimensional flowfields around lifting configurations. Several three-dimensional test cases have been considered to evaluate the stability, accuracy, and computational efficiency of this three-dimensional PNS scheme, and the results of this study are indeed very encouraging.

Solution Scheme

The coordinate system used for the present three-dimensional PNS scheme is a general curvilinear coordinate system (ξ_1,ξ_2,ξ_3) shown in Fig. 1. Also, a body-fixed orthogonal (Cartesian) coordinate system is chosen such that the origin of the Cartesian coordinate system is at the tip of the blunt nose, and the x axis is aligned with the axis of the body. The ξ_1 coordinate is along the body and is also the marching direction. The ξ_2 coordinate stretches from the body to the outer bow shock and lies in an axis-normal plane. The ξ_3 coordinate is measured in the crossflow direction from the windward pitch plane. In general, it is assumed that the (x,y,z) space is uniquely transformable to the (ξ_1,ξ_2,ξ_3) space through relations of the form

$$\xi_j = \xi_j(x,y,z) \tag{1}$$

The transformation given by Eqs. (1) is generally difficult to obtain. However, the metric derivatives for the inverse transformation can be easily obtained numerically. This information about the inverse-transform metrics is then used to determine the transformation Jacobians and the metric derivatives for the transformation given by Eqs. (1).

Governing Equations

The full Navier-Stokes equations governing the three-dimensional flow problem[23] can be nondimensionalized and rewritten in the following vectorial form:

$$(\boldsymbol{e}_j - \epsilon \boldsymbol{g}_j)_{,\mathrm{xj}} = \boldsymbol{p} \tag{2}$$

In our approach we choose the flowfield unknowns to be the density ρ, the density-velocity products ρu, ρv, and ρw, the static temperature T, and the pressure p. Thus the vector of unknowns is defined as

$$q = [\rho,\ \rho u,\ \rho v,\ \rho w,\ T,\ p]^T \tag{3}$$

Following the approach of Viviand[24] and Peyert and Viviand,[25] it can be shown that Eqs. (2) can be transformed into the general curvilinear coordinate system (ξ_j) as

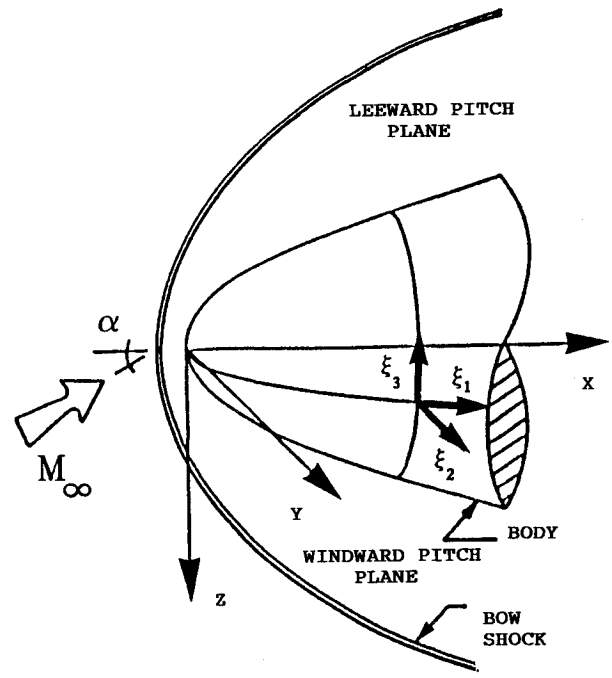

Fig. 1 General curvilinear coordinate system used.

$$(f_j - \epsilon s_j)_{,\xi j} = h \tag{4}$$

These equations are elliptic in ξ_1, ξ_2, and ξ_3 directions. If we neglect the diffusion and dissipation effects in the ξ_1 direction, we can write the parabolized Navier-Stokes version of Eqs. (4) in the following vectorial form[15-22]:

$$f_{j,\xi_j} - \epsilon s_{2\xi_2} \epsilon s_{3,\xi_3} = h \tag{5}$$

These five equations representing the differential conservation of mass, momentum, and energy are mathematically closed by using the equation of state for the gas mixure. For a perfect-gas model as well as an equilibrium-air gas model, this equation of state can be written in a nondimensional form as

$$\gamma_\infty p - Z^* \rho T = 0 \tag{6}$$

where $Z^* = 1$ for a perfect gas model and $Z^* = Z^*(p,T)$ for an equilibrium-air gas model.

Thermodynamic and Transport Property Data

For the perfect-gas model the mixture viscosity is obtained using the Sutherland formula,[23] and the specific-heat ratio is assumed to be a constant (1.4 for air). The mixture Prandtl number is also assumed fixed (0.72 for air), and the mixture thermal conductivity is obtained from the definition of mixture Prandtl number.

In the case of equilibrium chemically reacting air, the mixture thermodynamic and transport properties are provided in the form of a table. The dependant variables for these tabular data are chosen to be pressure p and temperature T. The thermodynamic properties involve the mixture enthalpy $h(p,T)$ and the mixture density (p,T) data and are based on the tabular data of Miner et al.[26] The transport properties involve the mixture viscosity data $\mu(p,T)$, the mixture thermal conductivity data $k(p,T)$, and the Prandtl number data $Pr(p,T)$. The viscosity and thermal conductivity data are based on the data developed by Peng and Pindroh.[27] The Prandtl number data were developed using this viscosity and thermal conductivity data, and the mixture specific-heat data were obtained by nu-

merically differentiating the enthalpy data of Miner et al.[26] The equilibrium-air thermodynamic and transport property table thus generated covers the temperature range of 10–15,000 K and the pressure range of 0.0025–15.849 atm. The pressure range of the thermodynamic property data of Miner et al.[26] is from 0.000025 atm to 39,810.72 atm; however, the reduced limits of the current table are due to transport property data of Peng and Pindroh.[27] The original transport property data of Peng and Pindroh[27] are in terms of a table of density and temperature. When these data were rearranged in terms of pressure and temperature, it was observed that outside the limits of 0.0025-15.849 atm the available data did not completely cover the temperature range of 10–15,000 K. Since a direct extrapolation of these data in terms of pressure may not be accurate, the current table was limited to this pressure and temperature range. It should be noted that this range adequately covers most of the flight regime in which the equilibrium-air effects may be important.

Local Linearization and Numerical Scheme

Let us denote the iteration level by the index n, so that the iteration at which we seek the solution is represented by the superscript $n+1$, and the previous iteration (the solution to which is known) is represented by the superscript n. If we assume that the solution at the $n+1$ level is close to the solution at the nth iteration, we can use a first-order Taylor-series expansion around the previous iteration. It should be noted that in evaluating the Jacobian matrices and doing the Taylor-series expansion around the nth iteration, we only consider the flowfield variables as the unknowns. Although the grid also changes from one iteration to the next, it is assumed that these changes are small and do not contribute to the Jacobian matrices. Thus, we see that by expanding the solution around the nth iteration and using two-point streamwise differencing, we can write Eqs. (5) as

$$(\boldsymbol{A}_1/\Delta\xi_1 - \boldsymbol{A}_0)^n \cdot \Delta\boldsymbol{q}^{n+1} + [(\boldsymbol{A}_2 - \epsilon\boldsymbol{M}_2)^n \cdot \Delta\boldsymbol{q}^{n+1}]_{,\xi_2} + [(\boldsymbol{A}_3 - \epsilon\boldsymbol{M}_3)^n \cdot \Delta\boldsymbol{q}^{n+1}]_{,\xi_3} = -(\boldsymbol{f}_{i,\xi_j} - \epsilon\boldsymbol{s}_{2,\xi_2} - \epsilon\boldsymbol{s}_{3,\xi_3} - \boldsymbol{h})^{j+1,n} = \boldsymbol{g}^{j+1,n} \tag{7a}$$

where

$$\Delta\boldsymbol{q}^{n+1} = \boldsymbol{q}^{j+1,n+1} - \boldsymbol{q}^{j+1,n} \tag{7b}$$

It has been shown by Bhutta and Lewis[15-22] that for the iterative process of Eqs. (7), the simple two-point streamwise differencing is conservative in the limit of convergence. This is not only important from a storage point of view, but it also gives the present scheme a significantly improved capability for treating strong compression discontinuities.

Fourth-Order Smoothing Effects

Equations (5) and (7) are elliptic in the ξ_2 and ξ_3 directions so that for second-order accuracy we use central-differenced approximations for all ξ_2 and ξ_3 derivatives. However, the use of central-differenced schemes is typically associated with solution oscillations.[4-9,15-22] This oscillatory behavior becomes more pronounced if the local velocities are small, so that the diagonal terms of the Jacobian matrices also become relatively small. To damp these solution oscillations, it is necesary to add some additional higher-order diffusion terms to Eqs. (5). However, in an iterative algorithm it is very important that these smoothing terms be consistently treated on both the implicit left-hand side and the explicit right-hand side of the differenced form of the governing equations. In noniterative PNS schemes,[4-9] this is not important because the solution is never driven to convergence. Consequently, classically, such smoothing operators were separated into a fourth-order explicit smoothing and a second-order implicit smoothing.[4-9]

In our earlier work,[15-22] we developed a second-order accurate fully implicit smoothing approach that is accurate and simple to use. In that approach the second-order smoothing effects were embedded in an explicit transformation between an intermediate (unsmoothed) solution and the final (smoothed) solution. However, some recent studies have shown that for long geometries with coarse crossflow grids, the second-order formulation can introduce excessive dissipation effects. In our present study, we have extended this smoothing formulation to fourth-order accuracy. In this approach we can write Eqs. (5) as

$$\boldsymbol{f}_{j,\xi_j}^{j+1,n+1} = \epsilon\boldsymbol{s}_{2,\xi_2}^{j+1,n+1} + \epsilon\boldsymbol{s}_{3,\xi_3}^{j+1,n+1} + \boldsymbol{h}^{j+1,n+1} + \pi_1(\boldsymbol{q})(\Delta\xi_2)^4 + \pi_2(\boldsymbol{q})(\Delta\xi_3)^4 \tag{8}$$

where the form of the vectors π_1 and π_2 is chosen such that (to fourth-order accuracy) we can rewrite Eqs. (6) in terms of an intermediate solution χ^{j+1} as

$$[f_i(\chi^{j+1})]_{,\xi_j} = \epsilon[s_2(\chi^{j+1})]_{,\xi_2} + \epsilon[s_3(\chi^{j+1})]_{,\xi_3} + h(\chi^{j+1}) + \mathcal{O}(\Delta\xi_2)^4 + \mathcal{O}(\Delta\xi_3)^4 \tag{9}$$

The actual solution at the $j+1$ step is related to this intermediate solution through the following fourth-order-accurate explicit transformations:

$$(\chi_1)^{j+1} = \chi^{j+1} - \chi_{,\xi_3\xi_3\xi_3\xi_3}\Delta\xi_3^4/16 \tag{10}$$

$$\boldsymbol{q}^{j+1} = \chi_1{}^{j+1} - \chi_{1,\xi_2\xi_2\xi_2\xi_2}\Delta\xi_2^4/16 \tag{11a}$$

An important advantage of this formulation is that the crossflow smoothing effects [Eqs. (10)] and the axis-normal smoothing effects [Eqs. (11a)] can be separately identified. Furthermore, the way these smoothing operations affect the individual flowfield variables can also be clearly seen. Being able to distinguish among these smoothing effects permits us to further enhance accuracy by restricting the axis-normal smoothing effects to only the pressure field. Thus, Eqs. (11a) are rewritten as

$$\boldsymbol{q}^{j+1} = (\chi_1)^{j+1} - [0,0,0,0,0,(\chi_{16})_{,\xi_2\xi_2\xi_2\xi_2}]^T\Delta\xi_2^4/16 \tag{11b}$$

where χ_{16} is the sixth element of the vector χ_1. In this manner, the axis-normal smoothing effects do not degrade the wall heat-transfer and skin-friction predictions.

Under-Relaxation and Pseudo-Unsteady Approach

Using a two-point streamwise differencing, central-differenced approximations in the ξ_2 and ξ_3 directions and after incorporating the higher-order smoothing terms, the final differenced equations corresponding to Eqs. (5) and (6) are written in the following block-pentadiagonal form:

$$(\boldsymbol{A}_1/\Delta\xi_1 - \boldsymbol{A}_0)^n \cdot \Delta\chi^{n+1} + [(\boldsymbol{A}_2 - \epsilon\boldsymbol{M}_2)^n \cdot \Delta\boldsymbol{q}^{n+1}]_{,\xi_2} + [(\boldsymbol{A}_3 - \epsilon\boldsymbol{M}_3)^n \cdot \Delta\boldsymbol{q}^{n+1}]_{,\xi_3} = -\omega(\boldsymbol{f}_{j,\xi_j} - \epsilon\boldsymbol{s}_{2,\xi_2} - \epsilon\boldsymbol{s}_{3,\xi_3} - \boldsymbol{h})^{j+1,n} = \boldsymbol{g}^{j+1,n} \tag{12a}$$

where

$$\Delta\chi^{n+1} = \chi^{n+1} - \chi^n \tag{12b}$$

and ω is an under-relaxation factor. This under-relaxation factor has values between 0 and 1, and it has been found to be very helpful in obtaining converged solutions for complex flowfields.[21] Typically, we use $\omega = 0.5$ for complicated flowfield calculations and $\omega = 1$ for simple flowfield calculations.

It should be noted that the right-hand side terms of Eqs. (12a) are the governing differential equations multiplied by the

factor ω, and they go to zero in the limit of convergence. As discussed by Bhutta and Lewis[15-21] and Bhutta et al.,[21] under these conditions the exact form of the left-hand implicit terms is of no great consequence except that it affects the convergence path of the solution. With this idea in mind we do not update the Jacobian matrices beyond the first iteration.

Boundary Conditions

The problem represented by the governing PNS equations is a split-boundary-value problem; i.e., the equations are hyperbolic-parabolic in the ξ_1 direction and elliptic in the ξ_2 and ξ_3 directions. Thus, in order to solve the problem completely we need initial conditions to be specified at the start of the marching procedure, boundary conditions to be specified at the wall and at the outer bow shock, and boundary conditions to be specified in the windward and leeward pitch planes (for flows with a pitch-plane of symmetry).

Initial Conditions

The initial conditions to start the PNS solutions were obtained from either appropriate VSL blunt-body solution schemes or an appropriate Navier-Stokes scheme. These blunt-body solutions were interpolated to obtain the starting solution at the initial data plane (IDP) for the three-dimensional PNS afterbody solution. Typically, for multiconic configurations we choose the starting location to be approximately 2-3 nose radii downstream of the nose stagnation-point location. However, in the case of a complex three-dimensional geometry, the IDP is generated at the most upstream nose-afterbody tangent point location.

Wall Boundary Conditions

The boundary conditions at the wall consist of six independent relations representing the nature of the gas mixture and the physical conditions at the wall. These conditions consist of no-slip boundary conditions, specified wall-temperature distribution, and equation of state and zero pressure derivative in the ξ_2 direction ($p_{,\xi_2} = 0$). This last boundary condition on the pressure derivative comes from a boundary-layer-type analysis performed at the wall.

Shock Boundary Conditions

The boundary conditions at the outer bow shock are, however, much more involved. These boundary conditions involve a fully implicit and crossflow-coupled shock-fitting approach, and the bow shock is predicted as the solution marches down the body. This shock-fitting scheme is discussed in more detail in the following sections.

Circumferential Boundary Conditions

Currently, our three-dimensional scheme is restricted to flows with a pitch plane of symmetry; i.e., the vehicle geometry is symmetric with respect to the pitch plane and there is no yaw. For such a case the boundary conditions in the windward and leeward pitch planes consist of reflective or symmetric boundary conditions. The symmetric and reflective boundary conditions used in the present study are based on the second-order crossflow boundary conditions used by Kaul and Chaussee[5] and Shanks et al.[8]

Predictor-Corrector Solution Scheme

When three-dimensional configurations are pitched at angle of attack, regions of strong crossflow can develop around the body. If the vehicle cross section is strongly three-dimensional, such regions of strong crossflow can even develop under small or zero angle-of-attack conditions. Typically, in these regions of strong crossflow the solution coupling in the crossflow direction is very important. If these coupling effects are not properly considered during the iterative solution, they can cause severe convergence difficulties. To address the problem of crossflow coupling, in this study we have used a new predictor-corrector solution scheme. We had originally developed this scheme to enhance solution stability under large-angle-of-attack conditions where fine crossflow grids were needed to accurately capture the flowfield details.[20,21] However, similar fine-grid situations also arise when modeling three-dimensional configurations.

The pentadiagonal system of equations to be solved can be written as

$$(\boldsymbol{D}\cdot\Delta\chi_{k-1,\ell}) + (\boldsymbol{A}\cdot\Delta\chi_{k,\ell-1}) + (\boldsymbol{B}\cdot\Delta\chi_{k,\ell}) + (\boldsymbol{C}\cdot\Delta\chi_{k,\ell+1}) + (\boldsymbol{E}\cdot\Delta\chi_{k+1,\ell}) = \boldsymbol{g}^{j+1,n} \tag{13}$$

The predictor-corrector scheme to solve this pentadiagonal system of equations is divided into three diffferent parts; namely, 1) the predictor step, 2) the shock solution, and 3) the corrector step. This solution scheme has been discussed in detail by Bhutta and Lewis,[20,21] and the following sections briefly describe the solution steps involved.

Predictor Step

In the predictor step, the implicit crossflow-coupling effects are neglected in favor of the axis-normal coupling effects. With this assumption, the equations for the predictor step become

$$(\boldsymbol{A}\cdot\Delta\chi^*_{k,\ell-1}) + (\boldsymbol{B}\cdot\Delta\chi^*_{k,\ell}) + (\boldsymbol{C}\cdot\Delta\chi^*_{k,\ell+1}) = \boldsymbol{g}^n \tag{14}$$

These equations are inverted from the body to the shock to develop a set of recursive relations between the predictor solution (χ^*) at each successive grid point in the body normal direction.

Crossflow-Coupled Shock Solution

Recently, we have also developed a new fully implicit and crossflow-coupled shock-fiting scheme.[20,21] In this shock-fitting scheme, the bow shock location is iteratively predicted as the solution marches down the body, and the numerical formulation is capable of treating different gas models in a unified manner.[20,21] Some of the important features of this bow shock-fitting approach follow.

1) Unlike earlier noniterative shock-propagation approaches,[8,9,28] this approach does not assume the flowfield behind the shock to be inviscid. This can be quite important when strong flowfield gradients exist behind the shock, as may be the case in the nose-dominated region and in regions where the bow shock starts to interact with the embedded shock waves (or compression waves) originating from the body.

2) Unlike the iterative shock-fitting approaches of Helliwell et al.[29] and Lubard and Helliwell,[30] this shock-fitting approach is for a general curvilinear coordinate system. Furthermore, it also does not increase the matrix size of the solution between the body and the shock.

3) Unlike an earlier iterative or noniterative bow shock-fitting scheme,[8,9,28-30] this shockfitting scheme does not neglect the crossflow coupling effects at the shock. This results in accurate and smooth shock shapes even when there are strong crossflow variations of the conditions behind the shock. This can be especially important when dealing with complex three-dimensional configurations where the three-dimensional nature of the body can interact with the bow shock and substantially distort it. Similar strong crossflow variations may also occur on simple configurations when they are pitched at large angles of attack.

In the bow shock-fitting scheme, it is assumed that from one iteration to the next, the shock points move along the ξ_2 grid line. This direction corresponds to the intersection of the $\xi_1 = \text{const}$ and $\xi_3 = \text{const}$ surfaces. This assumption considerably reduces the number of unknowns to be solved at the shock, and the final solution has only one additional unknown that completely defines the spatial movement of the shock point.

The smaller size of the unknowns is very important for a faster iterative solution and enhanced convergence characteristics of the overall implicit shock-prediction scheme. This simplification only represents a certain constraint on the direction in which the shock point moves and has no effect on the accuracy of the shock-crossing solution. To further simplify the numerical solution it is assumed that the metric derivatives $y_{,\xi 2}$ and $z_{,\xi 2}$ at the shock can be assumed as known from the previous iteration. Denoting the amount by which the shock point moves in the ξ_2 direction as Δ_s, the corresponding movement of the shock-point coordinates from one iteration to the next can be written as

$$(x_j)_s^{n+1} \simeq (x_j)_s^n + (x_{j,\xi_2})_s^n (\Delta)_s^{n+1} \tag{15}$$

The various velocity components at the shock surface can now be expressed in terms of the shock motion and shock coordinates. These velocity components are then used to write the five Rankine-Hugoniot shock-crossing equations (representing the conservation of mass, momentum, and energy). However, we actually have seven unknowns at the shock, written in a vectorial form as

$$q_s = (\rho, \rho u, \rho v, \rho w, T, p, \Delta)_s^T \tag{16}$$

Thus, two more equations are needed to close the system of equations at the shock. One of these additional equations is the equation of state of the gas, and the other equation is provided by applying the differential continuity equation behind the shock. As we see, no approximation other than the assumption of a Rankine-Hugoniot shock has been made. These equations are equally valid even if the conditions behind the shock are either viscous- or inviscid-dominated or if substantial flowfield gradients exist behind the shock. The dependance of all of the quantities appearing in these seven equations on the seven unknowns at the shock point q_s can be derived, and the equations are linearized around the previous iteration. The finite-differenced approximations to these equations involve central-differenced approximations for the ξ_3 derivatives and backward-differenced approximations for the ξ_1 and ξ_2 derivatives.[20,21]

Using the recursive relations of the predictor step, the inner flowfield solution can be expressed in terms of the shock-point solution. In this manner, the final system of equations to be solved at the shock takes the following block-tridiagonal form:

$$\boldsymbol{A}_k^n \cdot (\Delta \boldsymbol{q}_s)_{k-1}^{n+1} + \boldsymbol{B}_k^n \cdot (\Delta \boldsymbol{q}_s)_k^{n+1} \boldsymbol{C}_k^n \cdot (\Delta \boldsymbol{q}_s)_{k+1}^{n+1} = \boldsymbol{g}_k^n \tag{17}$$

This block-tridiagonal system of equations is solved using appropriate reflective and symmetric boundary conditions in the leeward and windward pitch planes of symmetry. This solution gives simultaneously the $\Delta \boldsymbol{q}_s{}^{n+1}$ vectors at each shock point ($k = 1,2,3,\ldots, KMAX$).

Using this shock-point solution and the recursive relations of the predictor step, we can now obtain the predicted solution vector χ^* for all interior grid points. At the same time, the x, y, and z coordinates of the updated shock-point locations to be used in the next solution iteration are determined using Eqs. (15).

Corrector Step

Just like the shock-point solution, the solution in the corrector step uses the recursive relations from the predictor step to eliminate the $(k,\ell-1)$ contributions in the difference molecule [see Eqs. (13)]. Then, assuming that the solution at the $(k,\ell+1)$ point is also known from the predictor step, one can reduce Eqs. (13) to only a coupled system of equations in the crossflow direction. This crossflow corrector solution can be written as[20,21]

$$\boldsymbol{D} \cdot \Delta \chi_{k-1,\ell} + (\boldsymbol{B} - \boldsymbol{A}\boldsymbol{R}_{k,\ell-1}) \cdot \Delta \chi_{k,\ell} + \boldsymbol{E} \cdot \Delta \chi_{k+1,\ell} \cong (\boldsymbol{g}^n - \boldsymbol{A} \cdot \boldsymbol{r}_{k,\ell-1}^n) - \boldsymbol{C} \cdot \Delta \chi_{k,\ell+1}^* \tag{18}$$

where χ^* is the predicted solution, and χ is the corrected solution. This implicit crossflow solution is obtained using plane-of-symmetry boundary conditions applied in the windward and leeward pitch planes. In this way the flowfield solution is marched from the shock to the body. This overall iterative process is repeated until the solution converges at all grid points, and then the solution moves on to the next marching step.

Grid-Generation Algorithms

In our study we have used different grid-generation schemes to better model the complex three-dimensional configurations. These grid-generation schemes can be classified as 1) parabolic grid generation, 2) body-normal grid generation, and 3) a modified body-normal grid generation. For convex three-dimensional shapes, these grid-generation schemes provide a fast and efficient way of generating reliable computational grids.

Parabolic Grid Generation

The parabolic grid-generation scheme used is based on the algorithm developed by Noack,[31] which we appropriately modified to suit our solution procedure. An important advantage of such a parabolic grid-generation scheme over a hyperbolic grid-generation scheme[28] is that the shock-point locations are specified by the user and not determined by the grid-generation scheme. For complex three-dimensional cross sections, however, our experience with parabolic grid generation shows that the possibility exists that, as we march down the body, the body-point locations may start to shift more rapidly than the coresponding shock-point locations. This typically arises when the body shape rapidly changes in the streamwise direction. This relative displacement between the body- and the shock-point locations introduces a sort of twist in the grid. When this grid twisting becomes large, it affects the accuracy and convergence characteristics of the numerical solution. This twisting effect becomes more pronounced when the shock-layer thickness is small, such as may occur around body corners and shoulders. One way of reducing this grid twisting is to use the same circumferential stretching at the shock as used at the body. Sometimes, however, even this approach is not adequate to avoid unnecessary grid twisting.

Body-Normal Grid Generation

The body-normal grid-generation scheme uses grid lines that are straight body normal in an axis-normal plane. A simple algebraic grid generation is then used to locate the grid points along these body-normal grid lines. This grid generation is faster than the parabolic grid-generation scheme, while at the same time it does not have the problem of grid twisting. However, with this straight body-normal grid generation sheme, abrupt changes may occur around relatively sharp body corners due to the rapidly changing crossflow body slopes.

Modified Body-Normal Grid Generation

The modified body-normal grid-generation scheme was developed specifically to address the grid-generation problems posed by bodies with relatively sharp corners in the crossflow direction. In this case the grids generated are body normal everywhere except in the corner region where the grid slopes are gradually varied to proide a smoothly changing grid. For convex three-dimensional shapes, this grid-generation scheme provides a fast and efficient way to generate accurate and well-behaved grids.

Results and Discussion

To evaluate the performance of our three-dimensional PNS scheme, we applied it to study the supersonic/hypersonic flow around two different lifting configurations. These cases are broadly classified as case 1 and case 2. In each case, both perfect-gas and equilibrium-air gas models were used to analyze the flowfield. The following sections present the results for these test cases.

Case 1 Calculations

The geometry used for these case 1 calculations is shown in Fig. 2. It consists of a spherically blunt elliptical cross section with a flat bottom. This vehicle has a nose radius of 0.1 in. and a total length of 50 *Rn*. This geometry description was developed by Weber[32] by using the QUICK geometry description program.[33] The foremost nose-afterbody tangent point of this geometry is at 0.778 *Rn*, and the side surface has a 7-deg compression corner between $x=20$ *Rn* and $x=25$ *Rn*. The freestream conditions used for these calculations are shown in Table 1. They consist of a Mach 20 flight at an altitude of 125,000 ft and an angle of attack of 5 deg. The wall temperature for these calculations was fixed at 2000 °R, and only fully laminar flow conditions were considered.

Several calculations were done to study this case, and they have been summarized in Table 2. Cases 1a-1e are for a perfect-gas model, whereas case 1f is for an equilibrium-air gas model. In all these grids, the grid spacing near the wall was kept at 0.01% of the local shock-standoff distance. It should be noted that only the case 1a calculations were carried over the entire body length whereas the calculations for cases 1b-1f were done for only the first 30 nose radii of the body length. The following sections show some of the important aspects studied using these calculations.

Perfect-Gas Flowfield Predictions

Figures 3 and 4 show the crossflow pressure contours at 30 *Rn* and 40 *Rn* along the body. These figures clearly show a strong embedded shock around the lower corner surface that is quite developed by $x=30$ *Rn*. By $x=40$ *Rn* this embedded shock starts to interact and impinge on the bow shock and in the process pushes the bow shock outward along the corner region. Figure 4 shows that even at this location the embedded shock wave is clearly visible in the contour plots. The overall results indicate that by the body end ($x=50$ *Rn*) the embedded

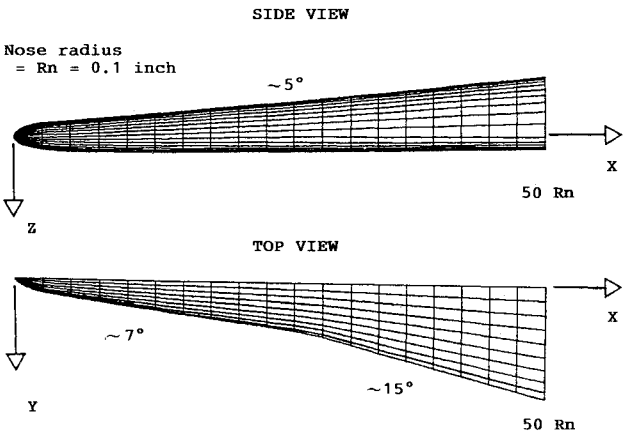

Fig. 2 Vehicle geometry for case 1.

Table 1 Freestream conditions

Quantity	Cases 1a-1f	Case 2a	Case 2b
Altitude	125.000	100.000	100.000
Mach number	20.000	10.000	5.000
Reynolds number	5.31E+3	2.15E+6	1.07E+6
Pressure, lbs/ft^2	7.760	23.1444	23.1444
Density, slug/ft^3	1.02E−5	3.28E−5	3.28E−5
Temperature, R	442.727	410.850	410.850
Velocity, ft/s	2.07E+3	9.94E+3	4.97E+3
Angle of attack, deg	5.000	25.000	5.000

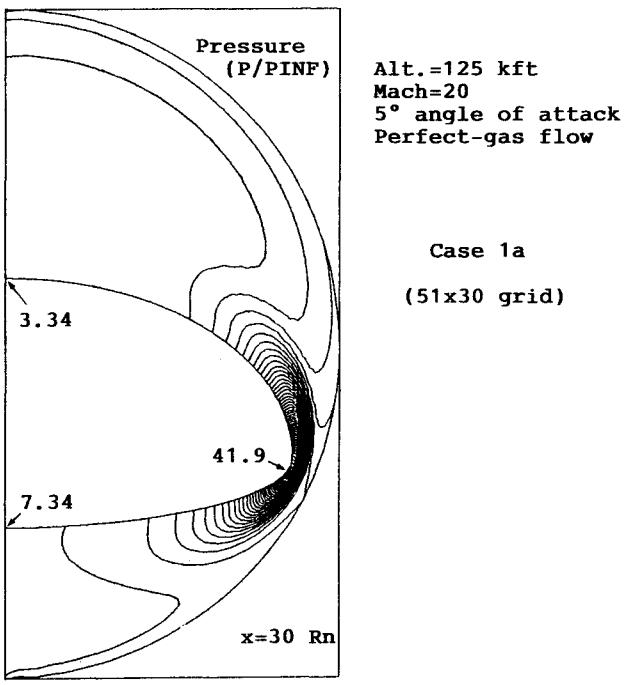

Fig. 3 Crossflow pressure contours for case 1a at $x=30$ *Rn*.

Table 2 Case parameters and computing times

Case	*x/Rn*, from-to	Grid used N1×N2×N3[a]	IBM-3090, min:s[b]	XMP-(4/8), min:s[c]	Cray-2, min:s[d]	Type of grid[e]	Gas model used[f]	Order of smoothing
1a	0.8-50	46×30×51	11:07	6:27	7:56	MBN	PG	Fourth
1b	0.8-30	36×30×31	5:11	2:04	3:27	MBN	PG	Fourth
1c	0.8-30	36×30×31	6:13	2:29	4:26	MBN	PG	Second
1d	0.8-30	36×30×31	6:11	2:28	4:25	BN	PG	Second
1e	0.8-30	36×30×31	7:17	2:55	5:12	PB	PG	Second
1f	0.8-30	36×30×31	5:57	2:23	4:15	MBN	EQ	Fourth
2a	5.0-30	26×30×31	6:07	2:27	4:22	MBN	PG	Fourth
2b	5.0-30	26×30×31	5:28	2:11	4:14	MBN	EQ	Fourth

[a]N1, N2, and N3 represent the number of grid points in the streamwise, axis-normal, and crossflow directions.
[b]Actual computing times on IBM 3090 (model 200 VF) with VS-compiler and scalar LEVEL = 3 optimization.
[c]Estimated computing times on Cray X-MP (4/8) with CFT77 compiler and auto vectorization.
[d]Estimated computing times on Cray-2 with CFT77 compiler and auto-vectorization
[e]MBN, BN, and PB represent the modified body-normal, the body-normal, and the parabolic grid-generation schemes.
[f]PG and EQ represent the perfect-gas and the equilibrium-air-gas models.

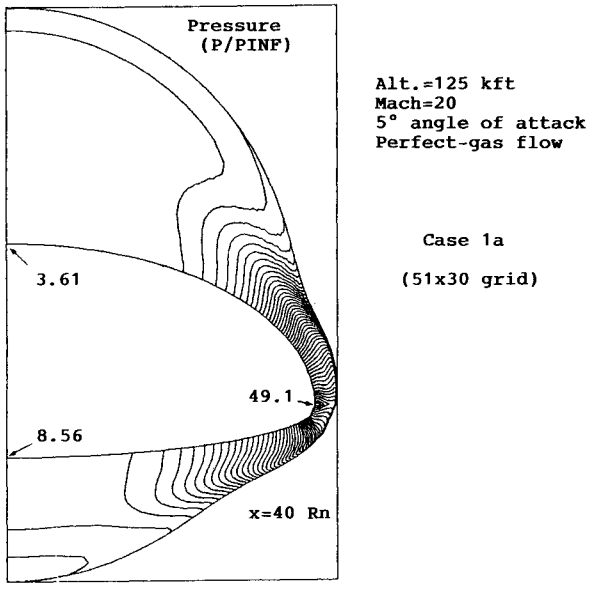

Fig. 4 Crossflow pressure contours for case 1a at $x = 40$ *Rn*.

shock merges with the bow shock; however, the shock surface still remains quite distorted.

Although not shown here, the corresponding crossflow distributions of the wall pressure and shock-standoff distance at the body end indicate a constant (almost two-dimensional) behavior along the flat bottom surface. However, unlike the wall-pressure distribution, the heat-transfer and skin-friction distributions along the bottom surface do not show a quasi-two-dimensional behavior. This is because in this case there are strong three-dimensional flowfield effects that are more visible in the wall heat-transfer and skin-friction predictions because, compared to the wall pressure, they are more sensitive quantities. Moreover, although the wall pressure along the flat bottom does show a quasi-two-dimensional behavior the predicted values are much higher due to the three-dimensional effects of the embedded crossflow shock.

The present results clearly demonstrate that, when studying such complex three-dimensional flows, an appropriate three-dimensional flowfield prediction scheme must be used. This is because, for many complex vehicle configurations some parts of the geometry may look like simple two-dimensional or axisymmetric regions and may tempt the application of simple two-dimensional or axisymetric-like solution approaches. The present results, however, indicate that even for the flow over such simple surface regions there are significant three-dimensional crossflow effects that need to be included. Furthermore, the wall heat-transfer and skin-friction distributions are more sensitive to these effects than either the wall pressure or the shock-standoff distance.

As shown in Table 2, it took nearly 11 min and 7 s to do the entire case 1a (15×30 grid) calculation on an IBM 3090 (Model 200 VF) machine. The estimated computing times for a typical Cray-2 machine and an X-MP (4/8) machine are also shown for comparison purposes. These computing times clearly show that, apart from being accurate and stable, the three-dimensional PNS scheme being presented is also computationally efficient and affordable.

Equilibrium-Air Effects

The effects of changing the gas model from perfect-gas to equilibrium chemically reacting air were studied using case 1b and case 1f calculations. Case 1b calculations were for a 31×30 grid using a perfect-gas model, and the case 1f calculations were from the same grid using an equilibrium-air gas model. The fourth-order smoothing formulation was used in each case.

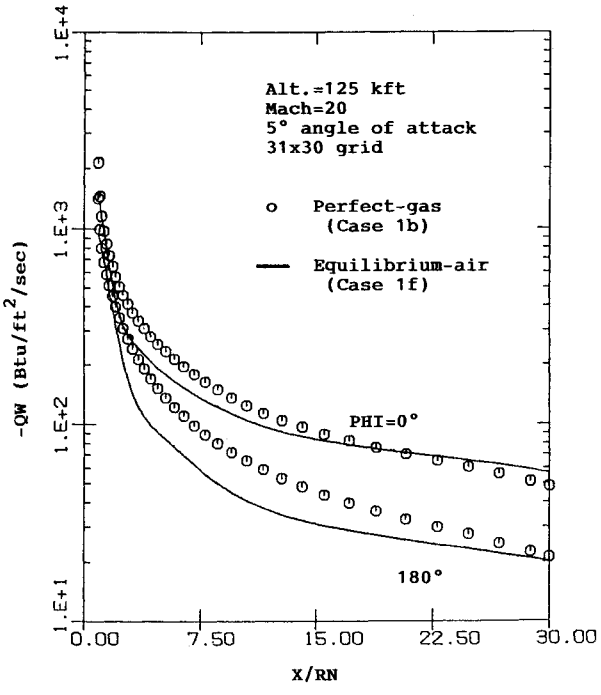

Fig. 5 Gas model effects on the axial distribution of wall heat-transfer rate for case 1.

Although not shown here, the results for this test case indicate that, along the windward surface, the perfect-gas and equilibrium-air predictions agree quite well. However, on the leeward side the perfect-gas pressures are as much as 40% higher. One of the main reasons for these differences in the predicted wall pressure is that, compared to the corresponding perfect-gas case (case 1b), the predicted equilibrium-air shock layer on the leeward side is as much as 40% thinner. Thus, due to the thicker leeside viscous region for the perfect-gas case, the corresponding wall pressure distribution shows a much larger viscous-induced pressure.

The axial distribution of wall heat-transfer rates for these calculations are compared in Fig. 5, and the corresponding crossflow distributions at $x = 30$ *Rn* are compared in Fig. 6. These results show that, compared to the perfect-gas predictions, the equilibrium-air predictions of the windward wall heat-transfer rates are as much as 20% lower in the forebody region, and they are as much as 15% higher in the afterbody region. The forebody wall heat-transfer predictions on the leeside with the equilibrium-air gas model are 30–40% lower than the perfect-gas case. In the afterbody region the perfect-gas and equilibrium-air predictions of the leeside wall heat-transfer rates are within 5% of each other. The predictions of the streamwise skin-friction coefficient are consistent with these wall heat-transfer results.

The computing times for these calculations are shown in Table 2. The case 1b perfect-gas calculations took 5 min and 11 s on the IBM 3090 (Model 200VF) machine, whereas the case 1f equilibrium-air calculations took 5 min and 57 s on the same machine. Thus, despite the accurate table look-up procedure involved, the equilibrium-air calculations with the present scheme took only 10–13% longer to do than the corresponding perfect-gas calculations. This shows that with the present three-dimensional PNS scheme, equilibrium-air calculations for even complicated three-dimensional configurations can be accurately done in an effective and affordable manner.

One of the important conclusions based on this study of the gas model effects is that for complex configurations, changing the gas model from perfect-gas to equilibrium chemically reacting air has a significant effect on the predicted flowfield. Previous experience with sphere cones at small to moderate (< 5 deg) angles of attack[15–19,22] had shown that the primary

effects of the gas model change were in the heat-transfer and skin-friction predictions. Our recent experience with large (20 deg) angle-of-attack flows over similar sphere cones[20,21] has shown that, under such conditions, substantial differences also start appearing in the predicted wall pessures and the bow shock shape. The present results show that pronounced effects of the gas model become evident even under moderate angle-of-attack conditions if the vehicle geometry has a complex three-dimensional shape.

Effects of Higher-Order Smoothing

As shown in Table 2, the effects of second-order and fourth-order smoothing were studied using the case 1b and case 1c calculations. The corresponding results showed that, in general, the predictions using the second-order and fourth-order formulations were in excellent agreement. Although not shown here, the maximum differences in the wall pressure, heat-transfer rate, and skin-friction was of the order of 1% or less. Furthermore, there was no identifiable effect on the predicted shock shape. However, there were important differences in the computing times required for these calculations (Table 2). The calculations with fourth-order formulation took 5 min and 11 s on IBM 3090 (model 200 VF), while the similar calculations with the second-order formulation took 6 min and 11 s. Thus, although the converged results did not change, with the fourth-order formulation the solution converged at a faster rate and resulted in a 20% reduction in the overall computing time required.

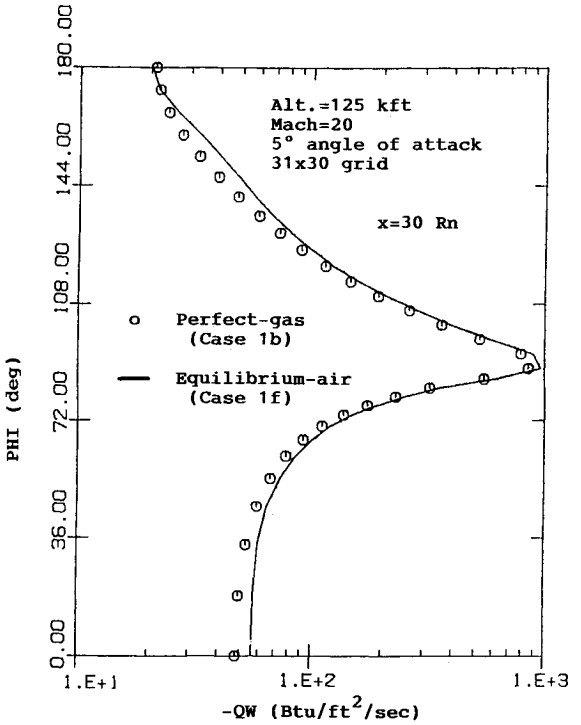

Fig. 6 Gas model effect on the crossflow distribution of wall heat-transfer rate for case 1.

Grid-Generation Results

In order to better model the geometry and the flowfield around it, in this case 1 study we have looked at the use of a parabolic grid generation (case 1e), a body-normal grid generation (case 1d), and a modified body-normal grid generation (case 1c). The crossflow grid distribution used at the surface in all cases was the same. Some sample grids generated at $x = 30$ Rn by using these schemes are shown in Fig. 7. As can be seen from these grids, for the case considered, all the grid generation schemes work reasonably well. There are, however, some important differences in the final grids generated. The parabolic grid shows a small amount of grid twisting developing around the lower body corner. This twist had started to develop even after efforts were made to match the crossflow grid distribution at the body and the shock. Furthermore, if the crossflow grid in the corner region were made any finer, there would be a substantial increase in grid distortion. The corresponding body-normal grid shows that although the grid twisting is eliminated, due to the rapidly changing body slopes around the corner region, the crossflow grid distribution away from the body was not good. The modified body-normal grid shows that the grid-twisting and the crossflow grid-spacing problems of the parabolic and the body-normal grids have been adequately resolved.

Although the modified body-normal and the parabolic grids shown look similar, the important difference is that farther down the body length the parabolic grids became excessively distorted, whereas the modified body-normal grids were still well behaved. Furthermore, the computing times given in

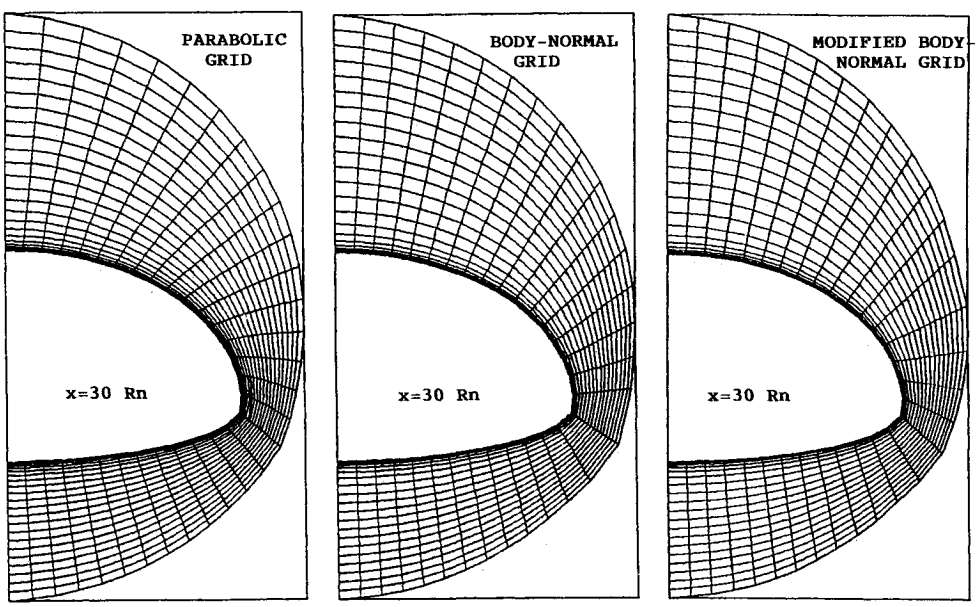

Fig. 7 Grid generation results for case 1 calculations.

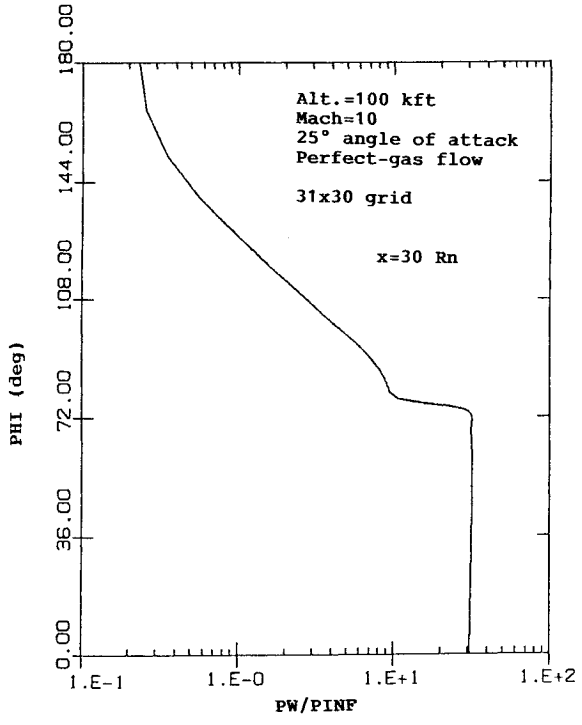

Fig. 8 Crossflow distribution of wall pressure for case 2a at $x=30$ *RN*.

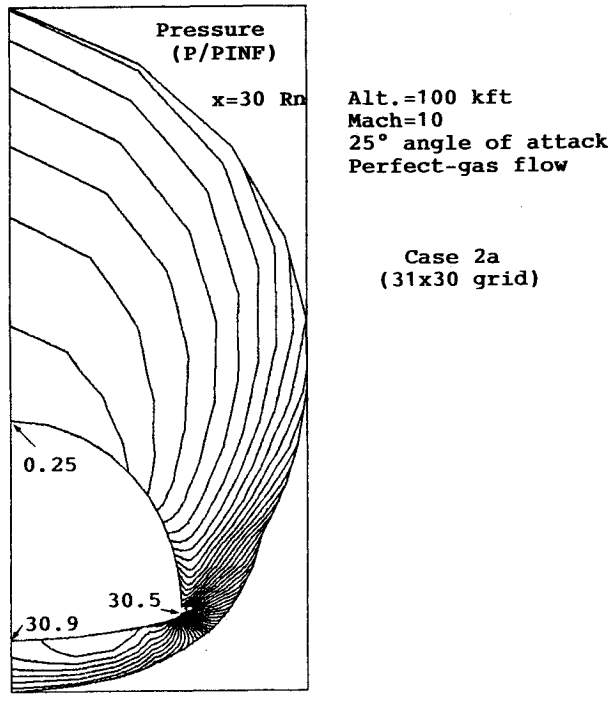

Fig. 9 Crossflow pressure contours for case 2a at $x=30$ *Rn*.

Table 2 show that the calculations with the body-normal and the modified body-normal grid-generation schemes took nearly 15–20% less time than the corresponding calculations using the parabolic grid-generation scheme. Thus, we see that our modified body-normal grid-generation scheme not only provides better quality grids for such geometries, but it is also faster and more efficient.

Effects of Crossflow Grid Refinement

The effects of crossflow grid refinement were studied using the 51-plane case 1a calculation and the 31-plane case 1b calculation. For the case 1b calculations, a relatively larger number of points were placed around the corner region to better model the flowfield changes in that region. Although not shown here the results showed that because of the additional clustering in the corner region, the 31-plane results agreed quite well with the 51-plane predictions. However, around the windward and leeward sides the 31-plane grid was much too coarse and considerably overpredicted the associated wall pressure, wall heat-transfer, and skin-friction values. Furthermore, even with the additional clustering, the 31-plane solution predicted a much thicker shock layer around the corner.

In general, the grid refinement studies showed that, for such complex lifting configurations, sufficiently fine crossflow grids are needed to adequately model the geometry as well as the flowfield around it. Because of the large three-dimensional flowfield effects, the common approach of using relatively coarse grids overall and only clustering them in regions of interest may not be a good approach for complex geometries. Because of this three dimensionality of the flowfield, inaccuracies in the coarse-grid regions may have a significant effect on the solution accuracy in the adjacent fine-grid region. Thus, sometimes, even if the local grid is adequate, the solution accuracy may not reflect it. And, even worse, some of the quantities may be reasonably predicted, whereas the others may not be (as was the case in the aforementioned shock-standoff results). Consequently, we feel that in such cases a general grid refinement of the solution domain may be a better and safer approach than a selective grid refinement of some regions at the expense of others.

Case 2 Calculations

The geometry used for the case 2 calculations was developed by Harris Hamilton, at NASA Langley Research Center, to model the flowfield around the Space Shuttle Orbiter.[34] The case 2a calculations are for a perfect-gas model, whereas the case 2b calculations are for an equilibrium-air gas model.

Perfect-Gas Predictions

The freestream conditions for these case 2a calculations are shown in Table 1 and correspond to a Mach 10 perfect-gas flow at an altitude of 100,000 ft and 25-deg angle of attack. The wall temperature for this case was kept fixed at 1800 °R, and the flow was considered to become fully turbulent at $x=5$ *Rn*. The solution in this case was carried down to $x=30$ *Rn*, where the wing tip starts to form. The grid used for these calculations consisted of a modified body-normal grid with 31 crossflow planes and 30 points between the body and the shock.

The crossflow distribution of the wall pressure at $x=30$ *Rn* is shown in Fig. 8, whereas the corresponding crossflow pressure contours at this location are shown in Fig. 9. For this case, the wall-pressure as well as the wall heat-transfer rate predictions along the lower surface have a marked quasi-two-dimensional character. The skin-friction predictions closely follow the heat-transfer predictions, and the shock-standoff distance shows the rapid thinning of the shock layer around the corner region. The computing time and the grid used for this case are given in Table 2, which shows that it took nearly 6 min and 7 s to do this case on an IBM 3090 (model 200VF) facility. These results and the corresponding computing times show that the present three-dimensional PNS scheme can even be used for large angle-of-attack flows over realistic three-dimensional configurations in an efficient and affordable manner.

Equilibrium-Air Predictions

The freestream conditions for these case 2b calculations are also shown in Table 1 and correspond to a Mach 5 equilibrium-air flow at an altitude of 100,000 ft and 5-deg angle of attack. The wall temperature for this case was also kept fixed at 1800 °R, and the flow was considered to become fully

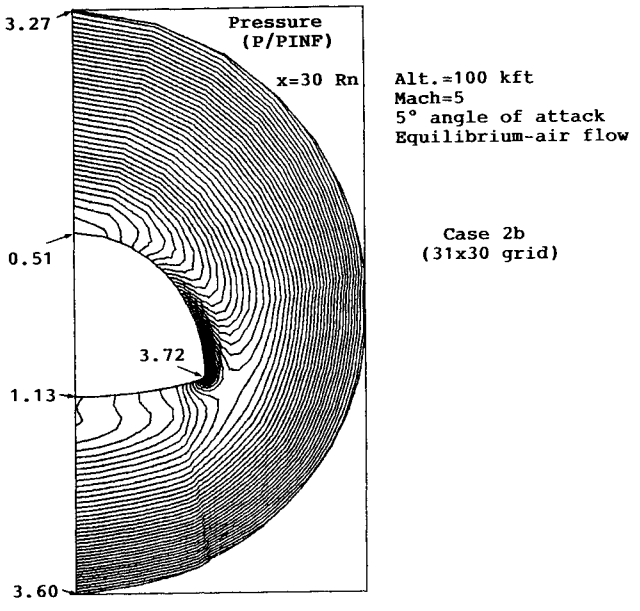

Fig. 10 Crossflow pressure contours for case 2b at $x=30$ *Rn*.

turbulent at $x=5$ *Rn*. Like the case 2a solution, this case 2b solution was also only carried down to $x=30$ *Rn*. The grid used for this calculation also consisted of a modified body-normal grid with 31 crossflow planes and 30 points between the body and the shock.

The crossflow pressure contours for the case at $x=30$ *Rn* are shown in Fig. 10. The corresponding axial and crossflow distributions of wall pressure and wall heat-transfer rate are quite smooth and well behaved. As shown in Table 2, this case took nearly 5 min and 28 s to do on an IBM 3090 (model 200VF) facility. This is indeed a relatively simple case compared to the case 1 and case 2a calculations presented earlier. However, this case was included to demonstrate the equilibrium-air capability of the present three-dimensional PNS scheme for supersonic or low hypersonic Mach numbers.

Conclusions

A new three-dimensional PNS scheme has been developed to study perfect-gas and equilibrium-air viscous hypersonic flows around complex three-dimensional configurations. Two different three-dimensional configurations were used to study the various aspects of this three-dimensional PNS scheme under realistic flight conditions. Studies were done to investigate the effects of gas model, grid-refinement, and different types of grid-generation schemes. The results of these studies substantiate the following comments:

1) Based on the PNS scheme of Bhutta and Lewis,[15-21] a three-dimensional PNS scheme for predicting perfect-gas and equilibrium-air hypersonic flows around three-dimensional configurations has been developed. This three-dimensional PNS scheme is unconditionally timelike in the subsonic as well as the supersonic flow regions and does not require the use of any sublayer approximation. The recently developed implicit shock-fitting and predictor-corrector solution schemes of Bhutta and Lewis[20,21] have been incorporated and used with a general curvilinear coordinate system.

2) A new fourth-order accurate smoothing approach has been developed to suppress numerical solution oscillations. This scheme is an extension of the earlier second-order-accurate approach of Bhutta and Lewis[15-21] and results in accurate and smooth flowfield predictions.

3) The results of the three-dimensional test cases considered show that substantial three-dimensional crossflow effects exist in the predicted flowfields. Even in regions where the body surface looks like a two-dimensional or an axisymmetric surface, there are considerable three-dimensional effects from the neighboring flowfield regions. Thus, simple quasi-two-dimensional or axisymmetric approximations for these flowfield regions are inadequate, and the overall flowfield is best predicted using an appropriate three-dimensional solution scheme.

4) Because of the strongly three-dimensional nature of the flowfields around complex lifting configurations, a localized grid refinement at the expense of the neighboring regions may not be an appropriate approach. In such cases the solution inaccuracies in the neighboring regions can exert a strong influence on the local solution accuracy. Thus, for such flowfield calculations, a more uniform grid refinement is a better and safer solution strategy.

5) Grid generation results show that for three-dimensional geometries with convex cross sections, a slightly modified variation of a body-normal grid-generation scheme shows the best characteristics. Such a grid generation scheme not only provides much better control over the grids generated than the parabolic grid-generation scheme, but it is also more efficient and took 20% less computing time.

6) Studies with prefect-gas and equilibrium-air gas models show that for complex configurations the type of gas model used has a substantial effect on the important flowfield quantities; e.g., the wall pressure, the shock-standoff distance, and wall heat-transfer and skin-friction predictions, etc. However, the results show that with the present three-dimensional scheme such equilibrium-air flowfield predictions can be accurately made in an efficient and affordable manner. Furthermore these equilibrium-air PNS calculations take only 10–15% more time than the corresponding perfect-gas predictions.

References

[1]Sahu, J., "Drag Predictions for Projectiles at Transonic and Supersonic Speeds," U. S. Army Ballistic Research Lab., Aberdeen Proving Ground, MD, BRL-MR-3523, June 1986.

[2]Richardson, P., "High-Speed Configuration Aerodynamic CFD," First National Aerospace Plane Technology Symposium, NASA Langley Research Center, Hampton, VA, May 1986.

[3]Rizk, Y. M., Scott, J. N., and Neuman, R. K., "Numerical Simulation of Viscous Supersonic Flows in the Vicinity of Embedded Subsonic or Axially Separated Regions; Volume I and Volume II," Air Force Flight Dynamics Lab., Wright Patterson AFB, OH, AFWAL-TR-83-3113, Nov. 1983.

[4]Weinacht, P., Guidos, B. J., Sturek, W. B., and Hodes, B. A., "PNS Computations of Spinning Shell at Moderate Angles of Attack and for Long L/D Finned Projectiles," U. S. Army Ballistic Research Lab., Aberdeen Proving Ground, MD, BRL-MR-3522, June 1986.

[5]Kaul, U. K. and Chaussee, D. S., "AFWAL Parabolized Navier-Stokes Coded: 1983 AFWAL/NASA Merged Baseline Version," Flight Dynamics Lab., Air Force Wright Aeronautical Lab., Wright-Patterson AFB, OH, AFWAL-TR-83-3118, Oct. 1983.

[6]Schiff, L. B. and Steger, J. L., "Numerical Simulation of Steady Supersonic Viscous Flows," AIAA Paper 79-0130, Jan. 1979.

[7]Vigneron, Y. C., Rakich, J. V., and Tannehill, J. C., "Calculations of Supesonic Viscous Flows over Delta Wings with Sharp Subsonic Leading Edges," AIAA Paper 78-1137, July 1978.

[8]Shanks, S. P., Srinivasan, G. R. and Nicolet, W. E., "AFWAL Parabolized Navier-Stokes Code: Formulation and User's-Manual," Air Force Flight Dynamics Lab., Wright Patterson AFB, OH, AFWAL-TR-823034, June 1979.

[9]Chaussee, D. S., Patterson, J. L., Kutler, P., Pulliam, T. H., and Steger, J. L., "A Numerical Simulation for Hypersonic Viscous Flows Over Arbitrary Geometries at High Angle of Attack," AIAA Paper 81-0050, Jan. 1981.

[10]Murray, A. L. and Lewis, C. H., "Hypersonic Three-Dimensional Viscous Shock-Layer Flows over Blunt Bodies," *AIAA Journal*, Vol. 16, No. 12, 1978, pp. 1279-1286.

[11]Thareja, R. R., Szema, K. Y., and Lewis, C. H., "Chemical Equilibrium Laminar or Turbulent Three-Dimensial Viscous Shock-Layer Flows," *Journal of Spacecraft and Rockets*, Vol. 20, No. 5, 1983, pp. 454-460.

[12]Thareja, R. R., Szema, K. Y., and Lewis, C. H. "Viscous Shock-Layer Predictions for Hypesonic Laminar or Turbulent Flows

in Chemical Equilibrium over the Windward Surface of a Shuttle-Like Vehicle," *Progress in Astronautics and Aeronautics,* Vol. 85, AIAA, New York, 1983.

[13]Thompson, R. A., Lewis, C. H., and Kautz, F. A., II, "Comparison Techniques for Predicting 3-D Viscous Flows Over Ablated Shapes," AIAA Paper 83-0345, Jan. 1983.

[14]Kim, M. D., Bhutta, B. A., and Lewis, C. H., "Three-Dimensional Effects upon Real Gas Flows Past the Space Shuttle," AIAA Paper 84-0225, Jan. 1984.

[15]Bhutta, B. A. and Lewis, C. H., "Low Reynolds Number Flows Past Complex Multiconic Geometries," AIAA Paper 85-0362, Jan. 1985.

[16]Bhutta, B. A., and Lewis, C. H., "An Implicit Parabolized Navier-Stokes Scheme for High-Altitude Reentry Flows," AIAA Paper 85-0036, Jan. 1985.

[17]Bhutta, B. A. and Lewis, C. H., "Prediction of Three-Dimensional Hypersonic Reentry Flows Using a PNS Scheme," *Journal of Spacecraft and Rockets.* Vol. 26, No. 1, 1989, pp. 4-13.

[18]Bhutta, B. A. and Lewis, C. H., "Numerical Solutions of the Bhutta-Lewis Model Problem," VRA, Inc., Blacksburg, VA, VRA-TM-86-03, Oct. 1986.

[19]Bhutta, B. A. and Lewis C. H, "Parabolized Navier-Stokes Predictions of High-Altitude Re-entry Flowfields," VRA, Inc., Blacksburg, VA, VRA-R-85-02, April 1985.

[20]Bhutta, B. A. and Lewis, C. H., "Three-Dimensional Hypersonic Nonequilibrium Flows at Large Angles of Attack," *Journal of Spacecraft and Rockets,* Vol. 26, No. 3, 1989, pp. 158-166.

[21]Bhutta, B. A. and Lewis, C. H., "PNS Predictions of Three-Dimensional Hypersonic Flows with Strong Crossflow Effects," AIAA Paper 88-2696, June 1988.

[22]Bhutta, B. A., Lewis, C. H., Kautz F. A., II, "A Fast Fully-Iterative Parabolized Navier-Stokes Scheme for Chemically-Reacting Reentry Flows," AIAA Paper 85-0926, June 1985.

[23]White, F. M., *Viscous Fluid Flow,* McGraw-Hill, New York, 1974, pp. 28-30.

[24]Viviand, H., "Conservative Forms of Gas Dynamics Equations," *La Recherche Aerospatiale,* No. 1, Jan.-Feb. 1974, pp. 65-68.

[25]Peyert, R. and Viviand, H., "Computations of Viscous Compressible Flows Based on the Navier-Stokes Equations," AGARD, AG-212, 1975.

[26]Miner, E. W., Anderson, E. C., and Lewis, C. H., "A Computer Program for Two-Dimensional and Axisymmetric Nonreacting Perfect Gas and Equilibrium Chemically Reacting Laminar Transitional and/or Turbulent Boundary Layer Flows," Virginia Polytechnic Institute and State Univ., Blacksburg, VA, VPI-E-71-8, May 1971.

[27]Peng, T. C. and Pindroh, A. L., "An Improved Calculation of Gas Properties at High Temperaure Air," Aerospace Division, The Boeing Co., Rept. D2-11722, 1962.

[28]Kaul, U. K. and Chaussee, D. S., "A Comparative Study of the Parabolized Navier-Stokes (PNS) Code Using Various Grid Generation Techniques," AIAA Paper 84-0459, Jan. 1984.

[29]Helliwell, W. S., Dickinson, R. P., and Lubard, S. C., "Viscous Flows Over Arbitrary Geometries at High Angle of Attack," AIAA Paper 80-0064, Jan. 1980.

[30]Lubard, S. C. and Helliwell, W. S., "Calculation of the Flow on a Cone at High Angle of Attack," R&D Associates Santa Monica, CA, Rept. RDA-TR-150, Feb. 1973.

[31]Noack, R. W., "Inviscid Flow Field Analysis of Maneuvering Hypersonic Vehicles Using the SCM Forumulation and Parabolic Grid Generation," AIAA Paper 85-1682, July 1985.

[32]Weber, D. D., private communication, July 1988.

[33]Vachris, A. and Yeage, L., "QUICK-GEOMERY User's Manual," Grumman Aerospace/Aerodynamic Section, Technical Data Rept. 393-74-1, 1974.

[34]Hamilton H. H., private communication, July 1988.

Walter B. Sturek
Associate Editor